

CORRELATED ANISOTROPIES IN THE COSMIC FAR-INFRARED BACKGROUND DETECTED BY *MIPS/SPITZER*: CONSTRAINT ON THE BIAS

G. LAGACHE¹, N. BAVOUZET¹, N. FERNANDEZ-CONDE¹, N. PONTHEIU¹, T. RODET², H. DOLE¹, M.-A. MIVILLE-DESCHÊNES¹, J.-L. PUGET¹

Draft version October 20, 2021

ABSTRACT

We report the detection of correlated anisotropies in the Cosmic Far-Infrared Background at 160 μm . We measure the power spectrum in the *Spitzer*/SWIRE Lockman Hole field. It reveals unambiguously a strong excess above cirrus and Poisson contributions, at spatial scales between 5 and 30 arcminutes, interpreted as the signature of infrared galaxy clustering. Using our model of infrared galaxy evolution we derive a linear bias $b = 1.74 \pm 0.16$. It is a factor 2 higher than the bias measured for the local *IRAS* galaxies. Our model indicates that galaxies dominating the 160 μm correlated anisotropies are at $z \sim 1$. This implies that infrared galaxies at high redshifts are biased tracers of mass, unlike in the local Universe.

Subject headings: infrared: galaxies –galaxies: evolution – (cosmology:) large-scale structure of universe

1. INTRODUCTION

The discovery of the Cosmic Far-Infrared Background (CIB) in 1996, together with recent cosmological surveys from the mid-infrared to the millimeter has revolutionized our view of star formation at high redshifts. It has become clear, in the last decade, that infrared galaxies contribute to a large part of the whole galaxy build-up in the Universe. Since the discovery of the CIB, new results on the identification of the sources contributing to the CIB, their redshift distribution, and their nature, are coming out at increasing speed, especially through multi-wavelength analysis (see for a review Lagache et al. (2005)). Stacking analysis are also very promising to probe the CIB source populations (e.g. Dole et al. (2006), Wang et al. (2006), Dye et al. (2007)). However, up to now, very little information is available on the clustering of infrared galaxies, although getting information on the clustering is essential to understand their formation process and to see how they relate to the other galaxy populations.

The first three-dimensional quantitative measurements of the clustering strength of Ultra and Hyper Luminous Infrared Galaxies (ULIRGs, HyLIRGs) at high redshifts ($z > 1.5$) have been made by Blain et al. (2004), Farrah et al. (2006) and Magliocchetti et al. (2007). These studies show that ULIRGs and HyLIRGs are associated with the most massive dark matter halos at high redshifts, unlike in the local Universe where the star formation is quenched in the densest environments. CIB anisotropy observations provide a powerful complement to direct high angular resolution observations of individual sources. CIB fluctuations measure, at large angular scales, the linear clustering bias and, at small angu-

lar scales, the nonlinear clustering within a dark-matter halo (Cooray & Sheth (2002)). They thus probe both the dark-matter halo mass scale and the physics governing the formation of infrared galaxies within a halo. However, up to now correlated anisotropies have never been firmly detected. In the far-infrared, detection of anisotropies is limited to the Poisson contribution (Lagache & Puget (2000), Matsuhara et al. (2000), Miville-Deschênes et al. (2002))³.

We report the detection of CIB correlated anisotropies at 160 μm in the *Spitzer* SWIRE Lockman Hole field and give a first constraint on the linear bias. The paper is organised as follow: data are presented in Sect. 2. The power spectrum is analysed in Sect. 3. Finally a summary and discussion are given in Sect. 4.

Throughout this paper we use the cosmological parameters $h = 0.71$, $\Omega_\Lambda = 0.73$, $\Omega_m = 0.27$. For the dark matter linear clustering we set the normalization to $\sigma_8 = 0.8$.

2. THE LOCKMAN HOLE SWIRE FIELD: MAP AND POWER SPECTRUM

SWIRE has surveyed 49 square degrees distributed over 6 fields in the northern and southern sky (Lonsdale et al. (2004)). The Lockman Hole is the largest field with the lowest cirrus emission. It covers about 10 square degrees at 160 μm .

2.1. Data reduction and map

Raw data were reduced using the Data Analysis Tool (Gordon et al. (2005)) version 2.71. We systematically removed each DCE (data collection event) after the stimulator flash to minimize the latency effect. We use the last calibration factor (44.7) to convert *MIPS* units to MJy/sr. Data were finally projected on a grid with 15.95 arcsecond pixels. The map is shown on Fig. 1. Further processings were necessary prior to measuring the power spectrum. We first needed to remove residual stripes. This has been done exactly in the same way as

¹ Institut d'Astrophysique Spatiale (IAS), Bâtiment 121, F-91405 Orsay (France); Université Paris-Sud 11 and CNRS (UMR 8617); [guilaine.lagache, nicolas.bavouzet, nestor.fernandez, nicolas.ponthieu, herve.dole, mamd, jean-loup.puget]@ias.u-psud.fr

² Laboratoire des signaux et systèmes (L2S), Supélec, 3 rue Joliot-Curie, 91190 Gif-sur-Yvette (France); Thomas.Rodet@lss.supelec.fr

³ Note however that Grossan & Smoot (2006) report the detection of the clustering signature at 160 μm .

in Miville-Deschênes & Lagache (2005). This paper shows that our method efficiently removed residual stripes without affecting the astrophysical signal. We then remove all sources with $S_{160} > 200$ mJy (200 mJy is the high reliability threshold, as detailed in Surace et al. (2005)). For this purpose we use DAOPHOT to detect the sources (the image was wavelet filtered prior to the detection). We then measure the fluxes using aperture photometry. After a fine centering on the sources, we integrate within $25''$. Sky values are estimated in an $[80''-110'']$ annulus. We compute the aperture correction – which is 2.02 – using an effective instrumental function (that we call PSF for Point Spread Function) measured directly on a *MIPS* 160 μm map. Using an effective PSF rather than the PSF computed using the STinyTim program⁴ is important to take into account the survey strategy. In the Lockman Hole SWIRE field, the signal-to-noise ratio was not high enough to accurately measure the PSF. We thus use the GTO/CDFS field in which the integration time is 6 times that in the Lockman hole SWIRE field. We checked that our measured fluxes at 160 μm were in very good agreement with the SWIRE DR2 catalog (better than 10% on average). On Fig 1 is shown the final map that will be used to compute the power spectrum.

2.2. Power Spectra

There are four contributors to the power spectrum at 160 μm : cirrus emission, Poisson (shot) noise from discrete unresolved sources, CIB clustering (if any), and instrumental noise. If the noise and the signal are not correlated, the measured power spectrum $P(k)$ follows:

$$P(k) = \gamma(k) [P_{\text{cirrus}}(k) + P_{\text{sources}} + P_{\text{clus}}(k)] + N(k) \quad (1)$$

where k is the 2D wavenumber ($k = \sqrt{k_x^2 + k_y^2}$, expressed in arcmin^{-1}), $P_{\text{cirrus}}(k)$, P_{sources} , $P_{\text{clus}}(k)$ and $N(k)$ are respectively the power spectrum of the dust emission, the shot noise from unresolved sources (constant), the clustering and the noise. The factor $\gamma(k)$ represents the power spectrum of the PSF. To isolate the astrophysical components, we have to determine $N(k)$ and $\gamma(k)$.

The noise power spectrum $N(k)$ is computed by subtracting two maps of exactly the same region as detailed in Miville-Deschênes et al. (2002). We construct two maps using the even and odd scans. As expected, $N(k)$ and $P(k)$ meet at small scales ($k \sim 1 \text{ arcmin}^{-1}$) where the signal is noise-dominated. The noise power spectrum $N(k)$ is subtracted from the raw power spectrum $P(k)$.

One of the critical issues is to correct the power spectrum from the PSF $\gamma(k)$. The PSF at 160 μm computed using the STinyTim program is very accurate but does not include any effect induced by the observing strategy. We have therefore also extracted directly the PSF from the data (as discussed in Sect. 2). The comparison of the power spectrum corrected by these two PSF is shown on Fig. 2. They are in very close agreement but we can notice that the effective PSF gives a better result (i.e. a flat power spectrum for $0.25 < k < 0.8 \text{ arcmin}^{-1}$, as expected from P_{sources}).

⁴ <http://ssc.spitzer.caltech.edu/archanaly/contributed/stinytim/>

The error bars (shown in Fig. 3) are estimated using a frequentist approach. Mock signal plus noise maps are generated and analysed with the same pipeline as for the data. This gives a set of power spectra of which we compute the covariance matrix. The diagonal elements of the covariance matrix are the errors on the measured power spectrum.

3. POWER SPECTRUM ANALYSIS

3.1. Adding low spatial frequency data to constrain the cirrus component

Several studies show that the cirrus component dominate the power spectra at large scales for $k < 0.01 \text{ arcmin}^{-1}$ (e.g. Miville-Deschênes et al. (2002; 2007)). With the SWIRE data only, in such a low interstellar dust column density field, P_{cirrus} cannot be constrained. Larger maps are needed. We therefore compute the power spectrum of a large ($\sim 200 \text{ Sq. Deg.}$) *IRIS/IRAS* 100 μm maps (Miville-Deschênes & Lagache (2005)). The SWIRE Lockman Hole field is embedded in this large *IRIS* map so that the average 100 μm dust emission is the same in the SWIRE and larger map (4% difference). Having the same average brightness is important since the normalisation of the cirrus power spectrum in the very diffuse region scales as I_{100}^2 (Miville-Deschênes et al. (2007)). We compute the power spectrum of the 100 μm map after removing the bright sources as in Miville-Deschênes et al. (2007). We keep only the largest scales ($k < 9 \cdot 10^{-3} \text{ arcmin}^{-1}$), where we have only the contribution from the cirrus component – the CIB being negligible at these very large scales – and multiply the power spectrum by the average dust emission color $(I_{160}/I_{100})^2$. The color has been computed using DIRBE and FIRAS data. We compute the average $|b| > 40^\circ$ spectrum of the dust emission correlated with the HI gas as in Lagache (2003). We then fit the peak of the dust emission spectrum to get the color. We obtain $I_{160}/I_{100} = 2.06$. If we take $|b| > 30^\circ$, the color varies by $\sim 10\%$. We show on Fig. 2 the 160 μm power spectrum derived from *IRIS* data together with the 160 μm *MIPS* power spectrum. The spectra agree impressively well. We can thus use this extended $P(k)$ to constrain the cirrus contribution. In the following, the two spectra are stitched so that we use one spectrum from $k \sim 0.001$ to 1 arcmin^{-1} .

3.2. Detection of an excess at intermediate scales: signature of correlated anisotropies

The cirrus component follows:

$$P_{\text{cirrus}}(k) = P_0 \left(\frac{k}{k_0} \right)^\beta \quad (2)$$

where P_0 is the power spectrum value at $k_0 = 0.01 \text{ arcmin}^{-1}$. P_0 and β are determined by fitting the power spectrum (see Sect. 3.3). We obtain $P_0 = (2.98 \pm 0.66) \times 10^6 \text{ Jy}^2/\text{sr}$ and $\beta = -2.89 \pm 0.22$. The normalisation can be converted at 100 μm using the 160/100 color given above; we obtain $P_0(100\mu\text{m}) = 7 \times 10^5 \text{ Jy}^2/\text{sr}$. Considering that the mean cirrus value at 100 μm in our field is $I_{100} = 0.51 \text{ MJy}/\text{sr}$, our measured $P_0(100\mu\text{m})$ and β are in excellent agreement with Miville-Deschênes et al. (2007). The power

spectrum of the cirrus component (Eq. 2) is displayed on Fig. 2. The measured power spectrum clearly has an excess of power w.r.t. the cirrus contribution for $k > 0.3 \text{ arcmin}^{-1}$. We interpret this strong excess as the signature of correlated CIB anisotropies.

We model the correlated anisotropies following Knox et al. (2001)⁵. Using the three-dimensional, linear-theory power spectrum of dark matter density fluctuations today, $P_M(k)$ the power spectrum of CIB anisotropies can be written as:

$$C_l^\nu = \int \frac{dz}{r^2} \frac{dr}{dz} a^2(z) \bar{j}^2(\nu, z) b^2 P_M(k)|_{k=l/r} G^2(z) \equiv P_{clus}(k) \quad (3)$$

where r is the comoving proper-motion distance, k the 3D wavenumber ($k = \sqrt{k_x^2 + k_y^2 + k_z^2}$, in Mpc^{-1}), $a(z)$ the scale factor, $\bar{j}(\nu, z)$ is the mean infrared galaxy emissivity per unit of comoving volume, and $G(z)$ is the linear theory growth function. ℓ is the angular multipole sets using the Limber approximation, $k = \ell/r$. We assume that the fluctuations in emissivity $\delta j/\bar{j}$ are a biased tracer of those in the mass and introduce the bias parameter b , that we assume independent of redshift and scale:

$$\frac{\delta j(\mathbf{k}, \nu, z)}{\bar{j}(\nu, z)} = b \times \frac{\delta \rho(\mathbf{k}, z)}{\bar{\rho}(z)} \quad (4)$$

where ρ is the dark matter density field. We compute the emissivity using the infrared galaxy evolution model of Lagache et al. (2004). This model, valid in the range 3-1000 μm , is in very good agreement with mid-IR to far-IR number counts, CIB observations, resolved sources redshift distributions and local luminosity functions and their evolution up to $z \sim 2$ (e.g. Lagache et al. (2004), Caputi et al. (2006), Dole et al. (2006), Frayer et al. (2006), Caputi et al. (2007)). Fixing the cosmology, the only unknown parameter in Eq. 3 is the bias b .

3.3. Measuring the bias

We fit simultaneously P_0 , β , b and $P_{sources}$ using the non-linear least-squares curve fitting mpfit program⁶. We obtain $P_0 = (2.98 \pm 0.66) \times 10^6 \text{ Jy}^2/\text{sr}$, $\beta = -2.89 \pm 0.22$, $b = 1.74 \pm 0.16$, and $P_{sources} = 9848 \pm 120 \text{ Jy}^2/\text{sr}$. P_0 and β have been discussed in Sect. 3.2. $P_{sources}$ agrees quite well with previous *ISOPHOT* determination at roughly the same S_{160} threshold (Matsuhara et al. (2000)). The fact that P_0 , β , and $P_{sources}$ are in very good agreement with previous measurements give us confidence in our measurement of the linear bias $b \sim 1.7$. It is well known that in the local Universe infrared galaxies are not biased tracers of the mass. For example, Saunders et al. (1992) found $b\sigma_8 = 0.69 \pm 0.09$ for *IRAS* galaxies. Assuming $\sigma_8 = 0.8$ gives $b = 0.86$. This bias is roughly comparable to the bias of the SDSS galaxies at $z \sim 0.1$ ($b \sim 1.1$, Tegmark et al. (2004)). We measure an average bias about 2 times higher in the CIB anisotropies. Figure 4 shows the predicted redshift contribution to the correlated anisotropies. At $k=0.05 \text{ arcmin}^{-1}$, anisotropies from $0.7 < z < 1.5$ infrared galaxies contribute for more $\sim 65\%$. Lower redshift galaxies contribute for less than

5%. This shows that infrared galaxies at $z \sim 1$ are much more biased (~ 2 times) than locally.

4. SUMMARY AND DISCUSSION

We presented the power spectrum measured in the *Spitzer*/SWIRE Lockman Hole field at 160 μm . It is very well reproduced by the contribution from three components, cirrus, correlated CIB, and Poisson noise. The cirrus and Poisson contributions are very close to previous measurements. We measure the linear bias, $b = 1.74 \pm 0.16$. This bias is likely to be that of infrared galaxies at $z \sim 1$ since $z \sim 1$ galaxies are dominating the contribution to the correlated CIB anisotropies (Fig. 4) and local galaxies are “anti-biased”. Such a bias is analog (but somewhat higher) to the bias of the red optical galaxy population at $z \sim 1$. For example, Marinoni et al. (2005) measured a bias of 1.6 at $z \sim 1.2$ for the red $(B - I) > 1.5$ galaxies in the VVDS. Blue galaxies at those redshifts are less biased with a relative bias between red and blue population of 1.4.

The very strong evolution of the bias (from ~ 1.7 at $z \sim 1$ to 0.86 at $z=0$) shows that as time progresses and the density field evolves, nonlinear peaks become less rare events and galaxy formation moves to lower-sigma peaks. Thus galaxies become less biased tracers of the mass density field. Moreover, for the infrared galaxy population it is likely that an additional mechanism contributes significantly to the “debiasing” at low redshift. Galaxies in dense environments are found to have suppressed star formation rates (thus no or low infrared emission) and early morphological types compared with those in the field. Environmental effects in particular are important in quenching the star formation through gas stripping (e.g. Postman et al. (2005)), though on some cluster outskirts, some star formation goes on (Duc et al. (2002), Coia et al. (2005)). The high bias found for infrared galaxies at $z \sim 1$ shows that star formation rates of galaxies are increasing with the environment (as also shown by e.g. Elbaz et al. (2007)). The “merger bias” is an alternative, but somehow physically linked, way of boosting the bias at high redshift. Clustering of objects that have undergone recent mergers can be enhanced relative to the clustering of individual halos of comparable masses (e.g. Furlanetto & Kamionkowski (2005); Wetzel et al. (2007)). It is known that the star formation in infrared galaxies is triggered to some extent by mergers in dense environments (at $z \sim 1$, 30-50% of luminous infrared galaxies are major mergers). Thus, the high measured bias may also point to “merger bias”.

This work is based on observations made with the *Spitzer* Space Telescope, which is operated by the Jet Propulsion Laboratory, California Institute of Technology under NASA contract 1407. This work benefited from funding from the CNES (Centre National d’Etudes Spatiales) and the PNC (Programme National de Cosmologie). We warmly thanks Asantha Cooray for helpful comments and suggestions.

⁵ Making a much more complex description of the correlated CIB anisotropies (as for example adding the contribution from the clustering within the same dark matter halo) and the bias is beyond

the scope of this paper.

⁶ <http://cow.physics.wisc.edu/~craigm/idl/idl.html>

REFERENCES

- Blain, A.W., Chapman, S.C., Smail, I., Ivison, R.J. 2004, *ApJ*, 611, 725
- Caputi, K.I., Dole, H., Lagache, G., et al. 2006, *ApJ*, 637, 727
- Caputi, K.I., Lagache, G., Yan, L., et al. 2007, *ApJ*, 660, 97
- Cooray, C.J., & Sheth, R. 2002, *Phys. Rep.*, 372, 1
- Coia, D., Metcalfe, L., McBreen, B., et al. 2005, *A&A*, 430, 69
- Dole, H., Lagache, G., Puget, J.-L., et al. 2006, *A&A*, 45, 417
- Duc, P.-A., Poggianti, B.M., Fadda, D., et al. 2002, *A&A*, 382, 60
- Dye, S., Eales, S.A., Ashby, M.L.N., et al. 2007, *MNRAS*, 375, 725
- Elbaz, D., Daddi, E., Le Borgne, D., et al. 2007, *A&A*, 468, 33
- Farrah, D., Lonsdale, C.J., Borys C., et al. 2006, *ApJ*, 643, 139
- Frayser, D.T., Farrah, D., Yan, L., et al. 2006, *AJ*, 131, 250
- Gordon, K.D., Rieke, G.H., Engelbracht, C.W., et al. 2005, *PASP*, 117, 503
- Grossan, B., & Smoot, G.F., 2006, *astro-ph/0604512*
- Furlanetto, S.R., & Kamionkowski, M. 2006, *MNRAS* 366, 529
- Knox, L., Cooray, A., Eisenstein, D., Haiman, Z. 2001, *ApJ*, 550, 7
- Lagache, G., Puget, J.-L., Dole, H. 2005, *ARAA*, 43, 727
- Lagache, G., Dole, H., Puget, J.-L., et al. 2004, *ApJS*, 154, 112
- Lagache, G. 2003, *A&A*, 405, 813
- Lagache, G., & Puget, J.-L. 2000, *A&A*, 355, 17
- Lonsdale, C., Polletta, M., Surace, J., et al. 2004, *ApJS*, 154, 54
- Magliocchetti, M., Silva, L., Lapi, A., et al. 2007, *MNRAS*, 375, 1121
- Miville-Deschênes, M.-A., Lagache, G., Puget, J.-L. 2002, *A&A*, 393, 749
- Miville-Deschênes, M.-A., & Lagache, G. 2005, *ApJS*, 157, 302
- Miville-Deschênes, M.-A., Lagache, G., Boulanger, F., Puget, J.-L. 2007, *A&A*, 469, 595
- Marinoni, C., Le Fèvre, O., Meneux, B., et al. 2005, *A&A*, 442, 801
- Matsuhara, H., Kawara, K., Sato, Y., et al. 2000, *A&A*, 361, 407
- Postman, M., Franx, M., Cross, N.J.G., et al. 2005, *ApJ*, 623, 721
- Saunders, W., Rowan-Robinson M., Lawrence A. 1992, *MNRAS*, 258, 134
- Surace, J.A., Shupe, D.L., Fang F., et al., “Data Release Paper for DR2”, accessible via: http://swire.ipac.caltech.edu/swire/astromers/data_access.html.
- Tegmark, M., Blanton, M.R., Strauss, M.A., et al. 2004, *ApJ*, 740, 606
- Wang, W.-H., Cowie, L.L., Barger, A.J. 2006, *ApJ*, 647, 74
- Wetzell, A.R., Cohn, J.D., White, M., Holz, D., Warren, M.S. 2007, *ApJ*, 656, 139

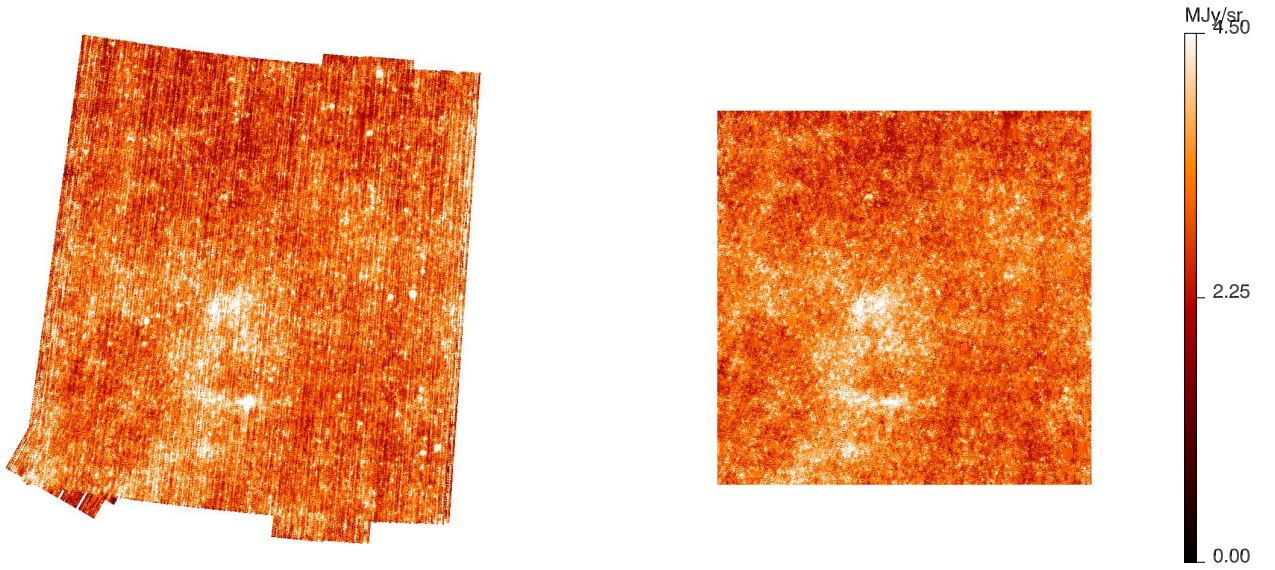


FIG. 1.— *Left*: 160 μm SWIRE map after standard data reduction. *Right*: Final map used to compute the power spectrum. Residual stripes have been corrected as in Miville-Deschênes & Lagache (2005). Sources with $S_{160} > 200$ mJy have been removed.

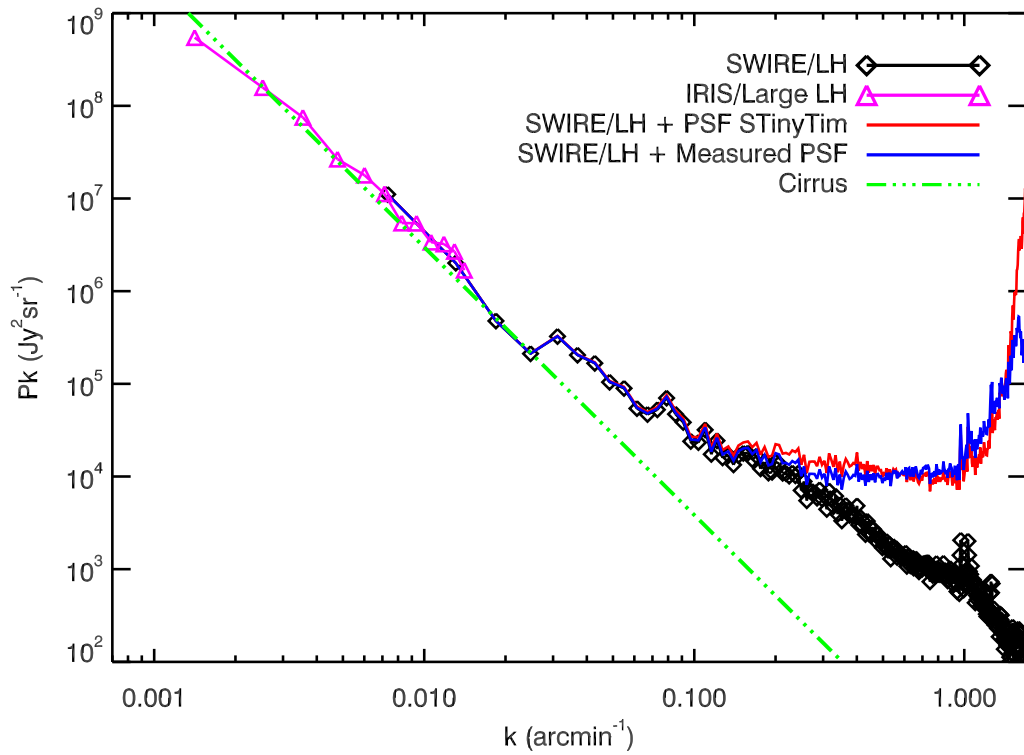


FIG. 2.— Total power spectrum measured in the Lockman Hole at 160 μm . In black (diamonds), the *MIPS*/*SWIRE* 160 μm power spectrum ($P(k) - N(k)$, see Eq. 1), in purple (triangles) the *IRIS/IRAS* enlarged Lockman Hole field power spectrum at 100 μm , scaled to the power spectrum at 160 μm using the 160/100 dust color measured at high latitudes ($|b| > 40^\circ$). In red and blue, the power spectra corrected from the *STinyTim* and measured PSF — $\frac{P(k) - N(k)}{\gamma(k)}$ —, respectively. The green dashed-3dotted line represents the best fit cirrus power spectrum, as computed in Sect. 3.3.

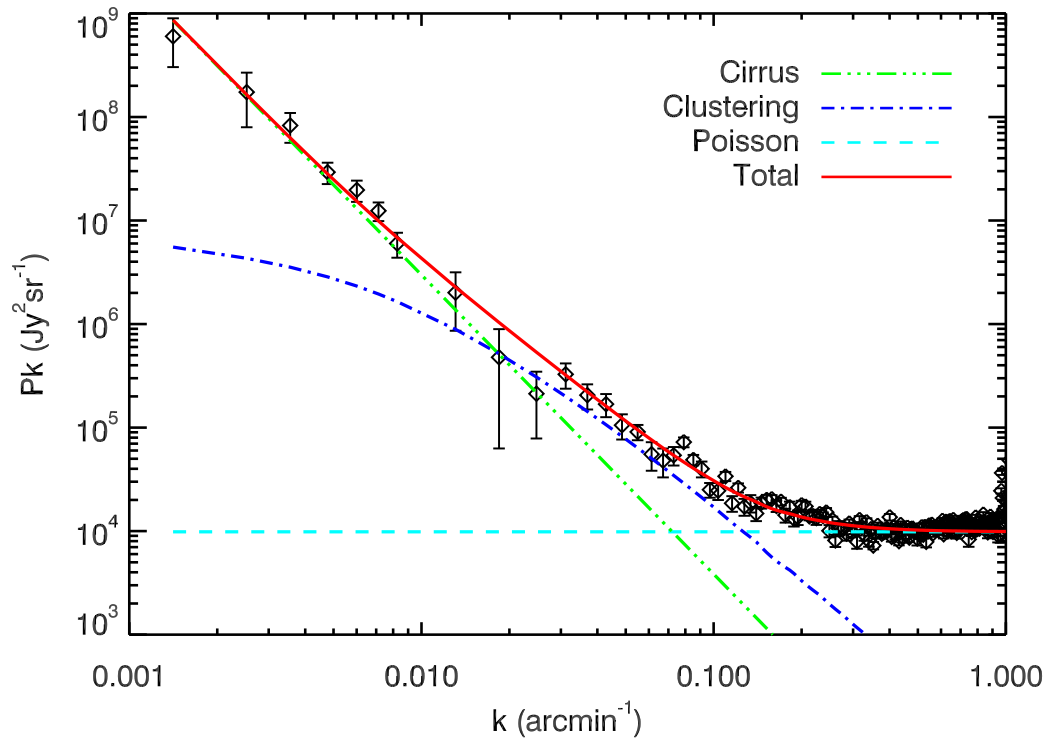


FIG. 3.— Power spectrum in the Lockman Hole at $160 \mu\text{m}$ (black diamonds with error bars) with the three components: cirrus (green dashed-3dotted line), clustering (blue, dashed-dotted line), Poisson (light blue, dashed line). The red continuous line is the sum of the three components.

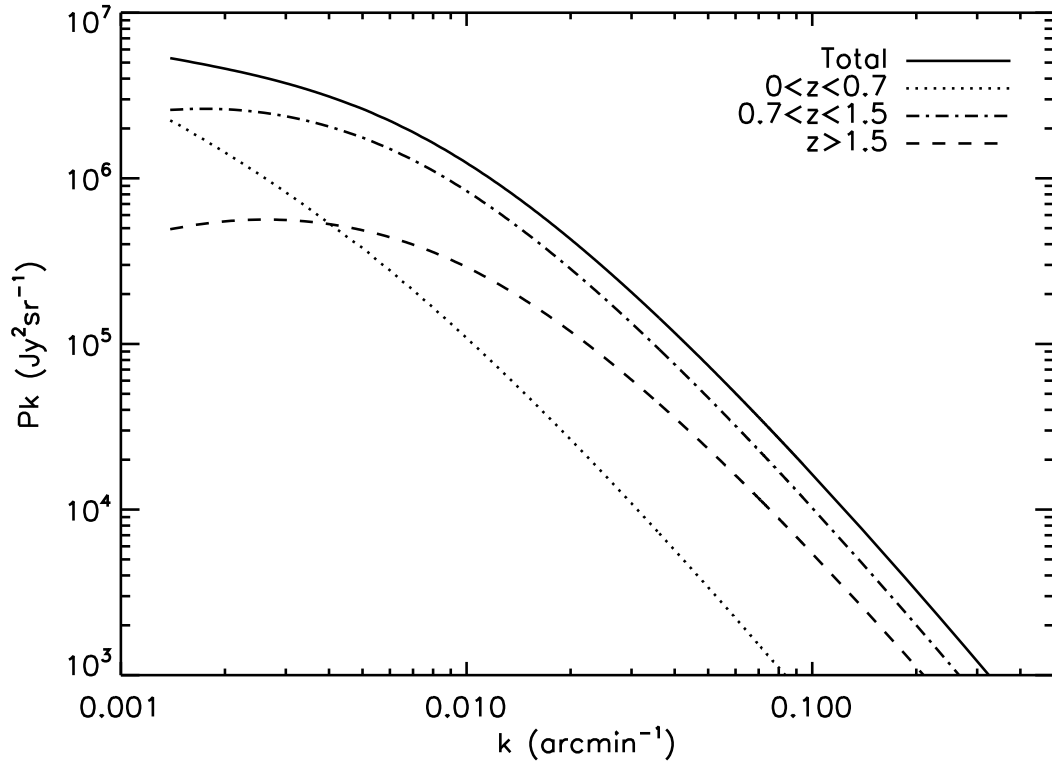


FIG. 4.— Redshift contribution to the correlated anisotropies at $160 \mu\text{m}$ for $b = 1.7$.